Supplementary Information (SI) for Journal of Materials Chemistry A.

Supplementary Materials for

Real-time evaluation of charge transfer patterns at buried ionotronic interfaces

Irum Firdous,[a^] Muhammad Fahim,[a^] Ruoxuan Ye[a], Johnny Sik Chun Lo,[b] Carol Sze Ki Lin,[b] Walid A. Daoud,[ac*]

[a] Department of Mechanical Engineering, City University of Hong Kong, Hong Kong, China

[b] School of Energy and Environment, City University of Hong Kong, Hong Kong, China

[c] Shenzhen Research Institute, City University of Hong Kong, Shenzhen, China

^ Equal contribution authors

*Corresponding author. Email: wdaoud@cityu.edu.hk.

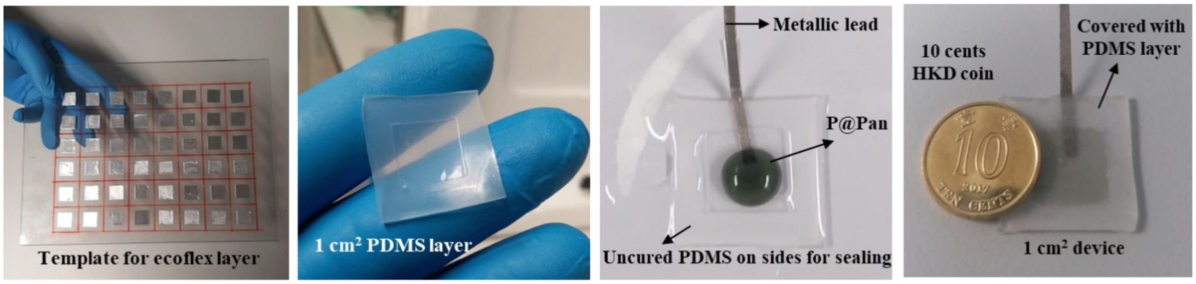

Fig. S1. Fabrication route of 1 cm^2 PVA@Pan induction layer based TEI.

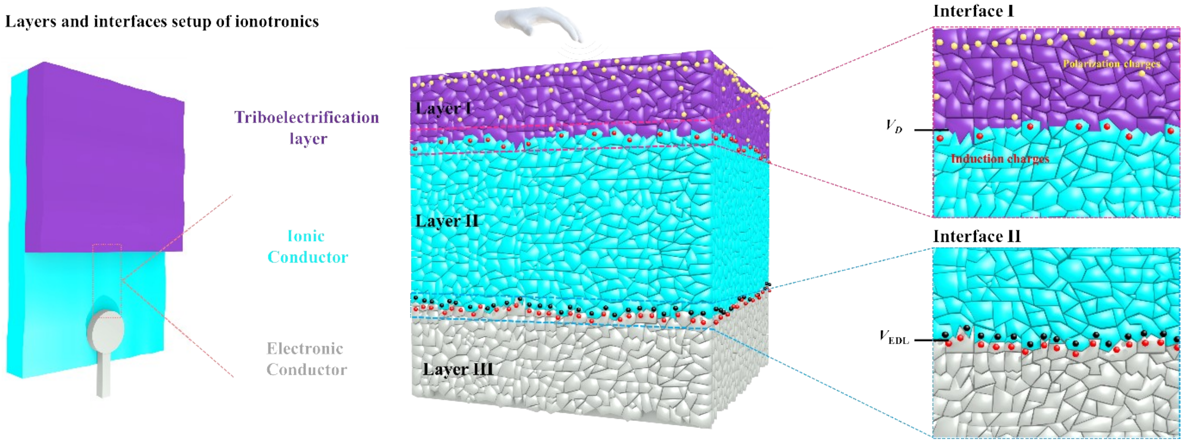

Fig. S2. Illustration of the origin of the output of ionotronics from two capacitors connected in series forming double layer capacitor and insulative layer capacitor.

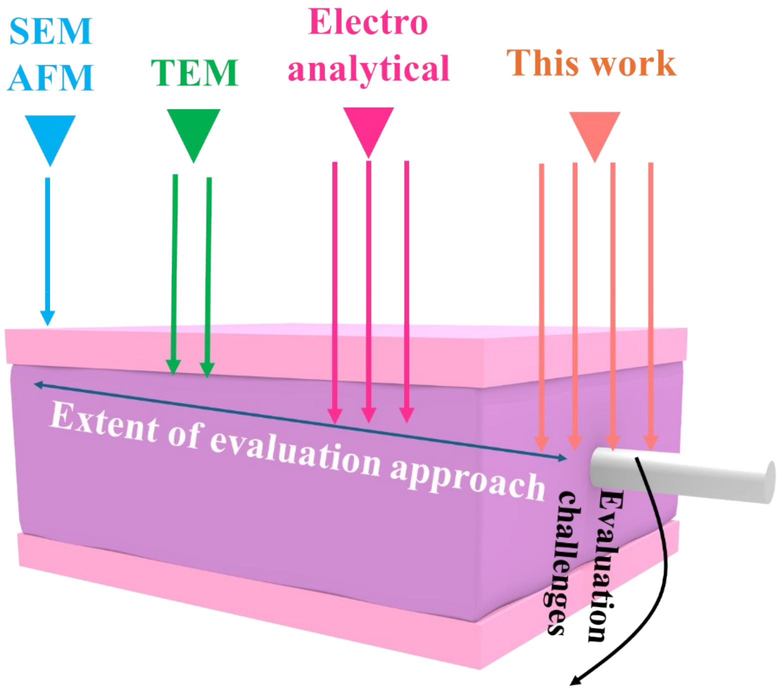

- **Single electrode system**
- **No dynamic reversible carrier ions**
- **Insulation-mediated buried interface**

Fig.S3. Comparison of the extent of evaluation techniques to study ionotronics interfaces.

Supplementary Note 1

Comprehensive Analysis of Charge Transfer Patterns via Nyquist Plots

The Nyquist plots presented in Figure S3 provide definitive evidence for the four distinct charge transfer patterns (Cases I-IV) in our TEI interfaces, revealing specific correlations with chemical species. The acidic media (Fig. S3a) displays a characteristic 45° Warburg slope at low frequencies transitioning to a nearly vertical line at high impedance values, confirming diffusion-limited proton (H^+) transport, corresponding to Case II. Salt systems (Fig. S3f) exhibit a unique impedance profile with logarithmic real impedance scaling, indicating mixed kinetic-diffusion control dominated by Na^+/Cl^- ion pairs that create frequency-dependent CPE behavior ($\alpha \approx 0.85$), representative of Case III. The oxidized metal response (Fig. S3c) shows a pronounced semicircle with extremely high charge transfer resistance ($R_{et} > 10\ M\Omega$), signifying Faradaic electrode degradation processes and correlating with Case IV, further validated by XPS-confirmed metal-anion bonding. In contrast, the polymer response (Fig. S3h) displays minimal impedance with near-vertical behavior in a significantly lower resistance regime (kΩ range versus MΩ for others), exemplifying the ideal capacitive behavior of Case I (true-EDL) with minimal charge transfer resistance ($R_{et} < 10\ \Omega$). The base, oxidant, and dopant/oligomer systems (Fig. S3d,b,g) show intermediate semicircular profiles, indicating various degrees of charge transfer limitation coupled with capacitive elements. The MWCNTs sample (Fig. S3e) exhibits a unique double-semicircle pattern, revealing interfacial and bulk transport processes occurring simultaneously.

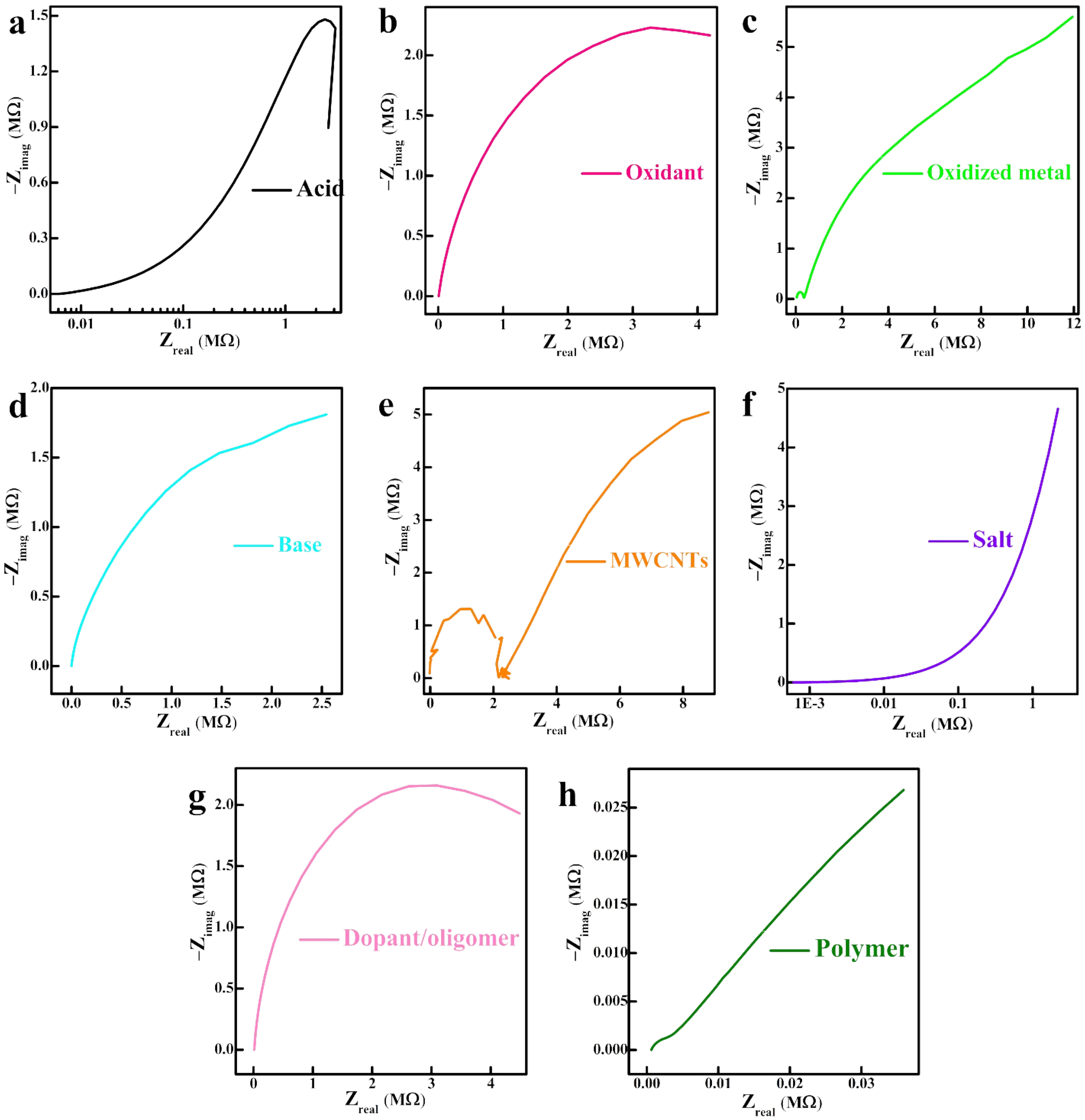

Fig. S4. Nyquist plots of eight material systems (a-h) showing distinct impedance behaviors correlated with specific chemical species in the TEI interfaces. Acidic media (a) exhibits Warburg diffusion (45° slope), salt-based systems (f) display mixed kinetic-diffusion control, oxidized metal interfaces (c) show high charge transfer resistance (12 MΩ), and polymer-stabilized systems (h) demonstrate near-ideal capacitive behavior. Equivalent circuits (insets) distinguish capacitive (CPE), resistive (Rct), and Warburg (W) components, validated by ZSimDemo modeling ($\chi^2 < 10^{-3}$). Cases I–IV correspond to true-EDL (h), diffusion-limited (a/f), charge transfer-limited (b/d/g), and Faradaic degradation (c) mechanisms, respectively.

Equivalent circuit fitting

Further, charge transfer pattern correlation with chemical species was evaluated through the equivalent circuit, as shown in Figure 1d and the relevant fitting values are provided in Table S1. The acid-based system with 45° Warburg slope (Rs=0.01 MΩ, Rct=1.2 MΩ) transitioning to a near-vertical capacitive line at higher impedance values, confirming diffusion-limited proton (H^+) transport with moderate CPE behavior (α=0.75), which corresponds to Case II in the classification. In contrast, the oxidant and dopant/oligomer systems display pronounced semicircular Nyquist profiles with elevated charge transfer resistance (Rct=3.8 MΩ and 3.5 MΩ respectively), indicating kinetic limitations at the electrode interface without significant diffusion components. The oxidized metal sample demonstrates the most severe charge transfer limitation with an extremely high Rct value of 12.0 MΩ and the lowest CPE-T (admittance, 0.05 μF), representing extensive electrode degradation consistent with Case IV where amphoteric species interact with the electrode surface. The base medium shows intermediate behavior with moderate Rct (2.5 MΩ) and improved capacitive character (CPE-P, CPE exponent =0.80), while the salt-based system presents unique logarithmic impedance scaling with the lowest solution resistance (Rs=0.001 MΩ) and strong diffusion control, aligning with Case III where oppositely charged ions precipitate at EDL. The MWCNTs sample reveals a distinctive double-semicircle pattern requiring a two-time constant equivalent circuit model, indicating separate interfacial and bulk transport processes occurring simultaneously. Most notably, the polymer system (Figure 4h) demonstrates near-ideal capacitive behavior (CPE-P=0.95) with minimal charge transfer resistance (Rct=0.03 MΩ) at significantly lower impedance ranges (kΩ rather than MΩ), exemplifying true-EDL formation (Case I) with efficient charge delocalization in the absence of reactive species. These distinct impedance signatures provide a quantitative framework for identifying chemical species in the induction layer and predicting device performance.

Table S1. Circuit fitting values for various induction layered materials.

Materials	Rs (MΩ)	Rct (MΩ)	CPE-T (μF)	CPE-P	Warburg
Acid	0.01	1.2	0.08	0.75	Yes
Oxidant	0.1	3.8	0.12	0.85	No
Oxidized metal	0.2	12	0.05	0.7	No
Base	0.05	2.5	0.15	0.8	No
MWCNTs	0.15	1.8	0.25	0.85	No
Salt	0.001	0.8	0.1	0.9	Yes
Dopant/oligomer	0.08	3.5	0.15	0.82	No
Polymer	0.005	0.03	0.35	0.95	No

Implications of CPE parameters in charge transfer patterns

The Constant Phase Element (CPE) parameters (Y_O, n) and their interplay with Warburg/diffusive components reveal critical insights into interfacial charge transfer mechanisms across the eight cases (acid, oxidant, oxidized metal, base, MWCNTs, salt, dopant/oligomer, polymer). In Case I (polymer), the near-ideal CPE behavior (n = 0.95, Y_O = 0.35 μF) reflects uniform charge distribution and minimal reactive species, thus enabling efficient double-layer capacitance (EDL) formation. This aligns with true-EDL systems where capacitive storage dominates (phase angle ~80° at 1 Hz). In contrast, Case II (acid) exhibits Warburg-dominated diffusion ($\sigma\_w \approx 1.2 \times 10^{-9}$ cm^2 s^{-1}) coupled with non-ideal CPE (n = 0.75, Y_O = 0.08 μF), indicating proton (H^+) mobility limitations and surface heterogeneity caused by acidic residuals.

Case III (salt) shows logarithmic Warburg scaling (Y_O = 0.10 μF, n = 0.90) with low solution resistance (R_s = 0.001 MΩ), highlighting Na^+/Cl^- ion pair diffusion as the rate-limiting step. The elevated n here suggests partial capacitive behavior due to ion accumulation at the interface. Case IV (oxidized metal) displays severe non-ideality (n = 0.70, Y_O = 0.05 μF) with high charge transfer resistance (R_ct = 12 MΩ), correlating with Faradaic corrosion processes (XPS-confirmed N–metal bonds) that disrupt capacitive charge storage.

Intermediate cases (oxidant, base, dopant) exhibit depressed semicircles (n = 0.80–0.85, Y_O = 0.12–0.15 μF), signifying mixed kinetic-diffusion control. For instance, oxidants induce charge transfer limitations (R_ct = 3.8 MΩ) due to redox-active species, while dopants/oligomers introduce localized dipole formation, reducing effective capacitance. The MWCNTs case (double semicircle, n = 0.85) demonstrates dual interfacial/bulk processes, with Y_0 = 0.25 μF reflecting enhanced surface area effects but compromised homogeneity.

These CPE trends directly correlate with material-specific charge transfer:

- High n (≥0.90): Near-ideal EDL formation (polymer, salt)
- Low n (≤0.75): Severe heterogeneity or Faradaic interference (acid, oxidized metal)
- Intermediate n (0.80–0.85): Distributed time constants from reactive species or rough interfaces

The effective capacitance (*C_eff*), derived via $C\_eff = Y_0(\omega\_max'')^{n-1}$, further quantifies performance. For example, the polymer's *C_eff* ≈ 0.33 F m^{-2} (vs. 0.08 F m^{-2} for acid) confirms its superior charge storage. These insights enable targeted material design: minimizing CPE deviation ($n \rightarrow 1$) through surface passivation or reactive species removal optimizes capacitive efficiency for applications, such as neuromorphic interfaces or energy storage.

Supplementary Note 2

Spectral excitation assignment of Pan

The UV-Vis spectrum of the polyaniline (Pan) has two characteristic peaks at 308–333 nm and 430–460 nm corresponding to π-π* and polaron-π* transition, respectively, indicating the conductive emeraldine state of Pan. Also, the intrinsic peak of Pan at 630 nm is converted to a free carrier tail commencing at 600 nm (Figure S5a), demonstrating longer conjugation of the Pan chain for induction of electron delocalization. The IR spectrum of Pan shows characteristic peaks at 1045 cm^{-1}, 1285 cm^{-1}, 1484 cm^{-1}, 1562 cm^{-1}, and 3225 cm^{-1} corresponding to S–O, C–N, benzenoid ring, quinoid ring, and N–H stretching, which endorse the conductive emeraldine salt state chemical structure of synthesized Pan, Figure S5b.

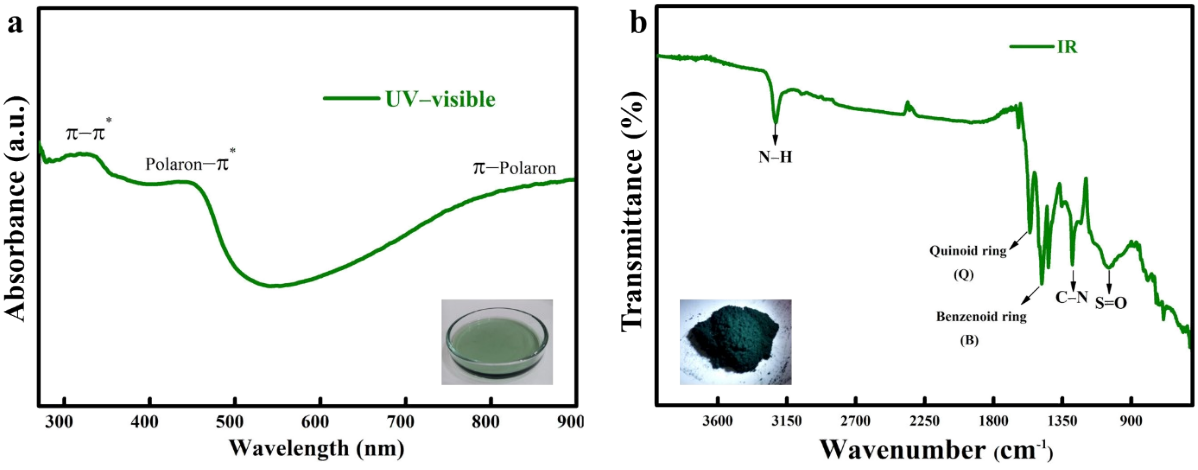

Fig. S5. (a) UV-Visible absorbance and (b) IR transmittance spectrum of polyaniline fabricated via interfacial polymerization, insets show the solution and solid forms of prepared polyaniline.

Supplementary Note 3

Spectral excitation assignment PVA@Pan

The UV-Visible spectrum of PVA shows two characteristic peaks at 282 nm and 337 nm attributed to π-π* transition in C=C and n-π* transition in C=O. In PVA@Pan the π-π* transition occurs at 282 nm, which is blue-shifted from pristine Pan π-π* transition at 318 nm, endorsing the copolymerization of PVA@Pan. Similarly, the n-π* transition for PVA@Pan occurs at 431 nm, which is red-shifted from the n-π* transition of pristine PVA at 337 nm. Further, PVA@Pan$_{\text{interfacial}}$ shows an intrinsic peak of Pan at 630 nm, which demonstrates the retention of longer conjugation for the induction of electron delocalization, Figure S 6a. The FTIR spectrum of PVA shows characteristic bands at 845 cm^{-1} and 1600 cm^{-1} attributed to C–H and C=O stretch, Figure S 6b. The hydroxyl peak is shifted to 3640 cm^{-1} and beyond representing free, non-bounded state of O–H. The small peak at 3000 cm^{-1} corresponds to an asymmetric CH_2 stretch. The spectra of Pan show characteristic peaks at 1160 cm^{-1}, 1270 cm^{-1}, 1517 cm^{-1}, and 1610 cm^{-1} corresponding to S–O, C–N, benzenoid ring, and quinoid ring. The band shifts to a higher wavenumber compared to pristine Pan (Figure S 5b) and the presence of free hydroxyl beyond 3560 cm^{-1} endorses the copolymerization with PVA.

The spectral and mechanical properties confirm that the copolymerization of Pan and PVA reinforces the mechanical strength and enhances the triboelectric property of PVA, Figure S 6c.

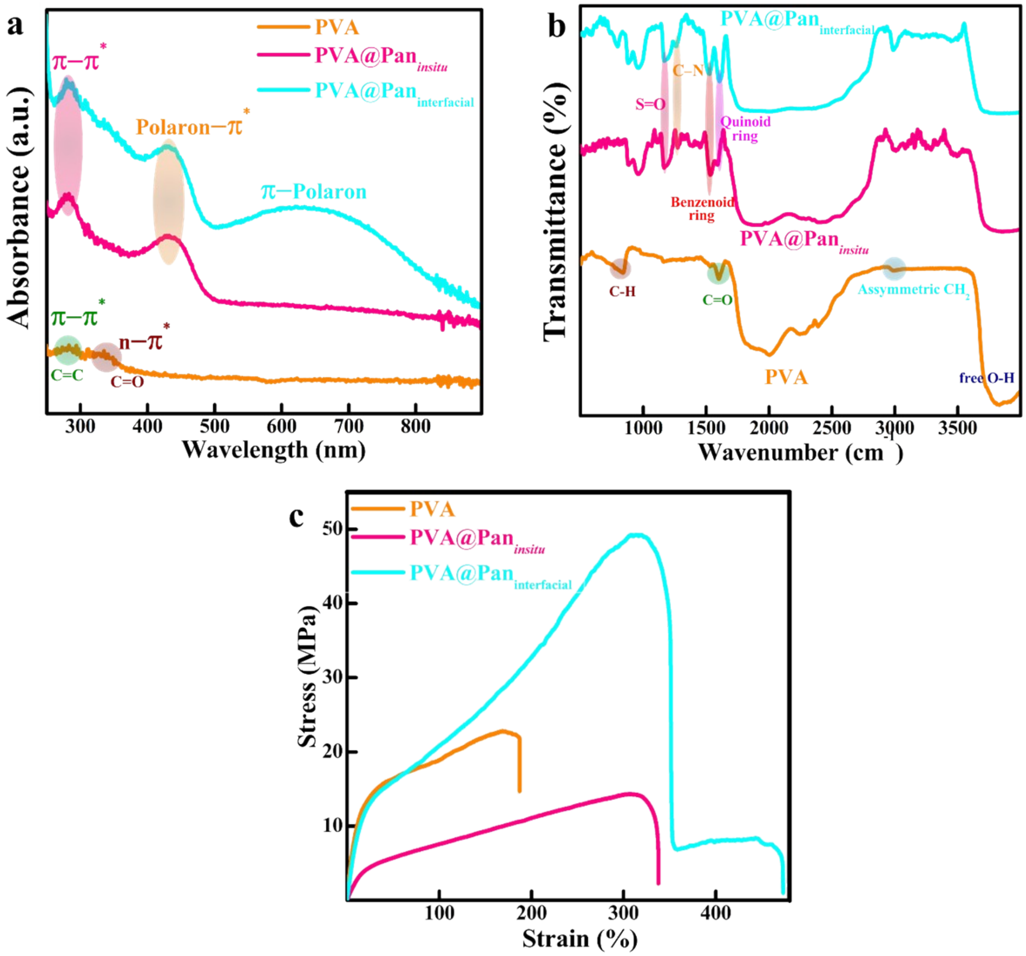

Fig. S6. Structure evaluation of the induction layer. Properties of pristine PVA (control), PVA@Pan$_{insitu}$ (pseudo-EDL), and PVA@Pan$_{\text{interfacial}}$ (true-EDL) induction layer: (a) UV-vis absorption spectra, (b) IR transmittance spectra, and (c) stress-strain profile.

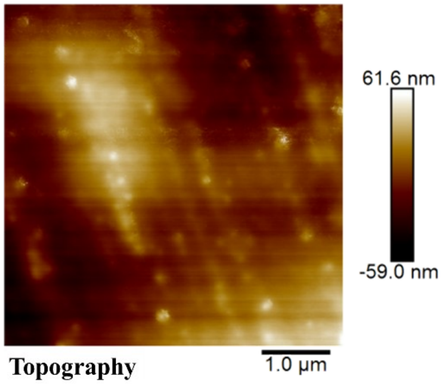

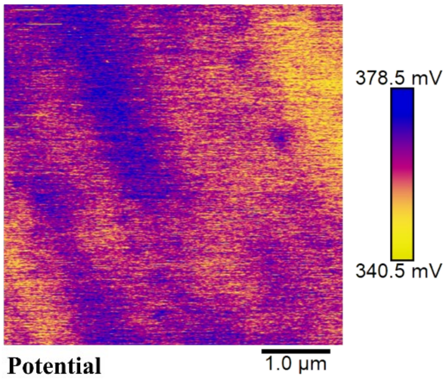

Fig. S7. KPFM topography and its corresponding potential mapping (25 µm^2) of pristine PVA film.

Supplementary Note 4

XPS Analysis of Degradation Mechanisms in Pseudo-EDL Devices

The XPS spectra provide compelling evidence for the specific degradation mechanisms in pseudo-EDL devices, Figure S8. The survey spectrum reveals distinct chemical differences between true-EDL and pseudo-EDL systems, with high-resolution scans of the N 1s and S 2p regions providing crucial insights into the reactive species responsible for electrode corrosion.

Most significantly, the pseudo-EDL sample exhibits a pronounced S 2p peak at approximately 168 eV, characteristic of sulfate/sulfonic acid species (SO_4^{2-}/HSO_4^{-}), which are entirely absent in the true-EDL sample. This confirms that residual H_2SO_4 from the oxidative polymerization of aniline remains trapped within the PVA@Pan insitu matrix. These acidic residuals create a corrosive microenvironment at the electrode-induction layer interface, leading to progressive degradation through sulfate-induced oxidation of the electrode.

The N 1s region further reveals important differences, with pseudo-EDL showing an intense peak at ~399-400 eV, indicating high concentrations of unreacted/partially oxidized aniline oligomers. These species, containing protonated amine and imine nitrogen atoms, contribute to degradation through two mechanisms: (1) direct chemical interaction with metal electrodes forming metal-N complexes, and (2) creation of localized pH gradients that accelerate corrosion processes.

Together, these spectroscopic data explain the observed performance deterioration in pseudo-EDL devices over 50 days, where trapped synthesis residuals (H_2SO_4 and aniline oligomers) continuously react with electrode materials. In contrast, the true-EDL approach, with its separate synthesis and subsequent layer formation, minimizes these reactive residuals, resulting in superior long-term stability and consistent performance.

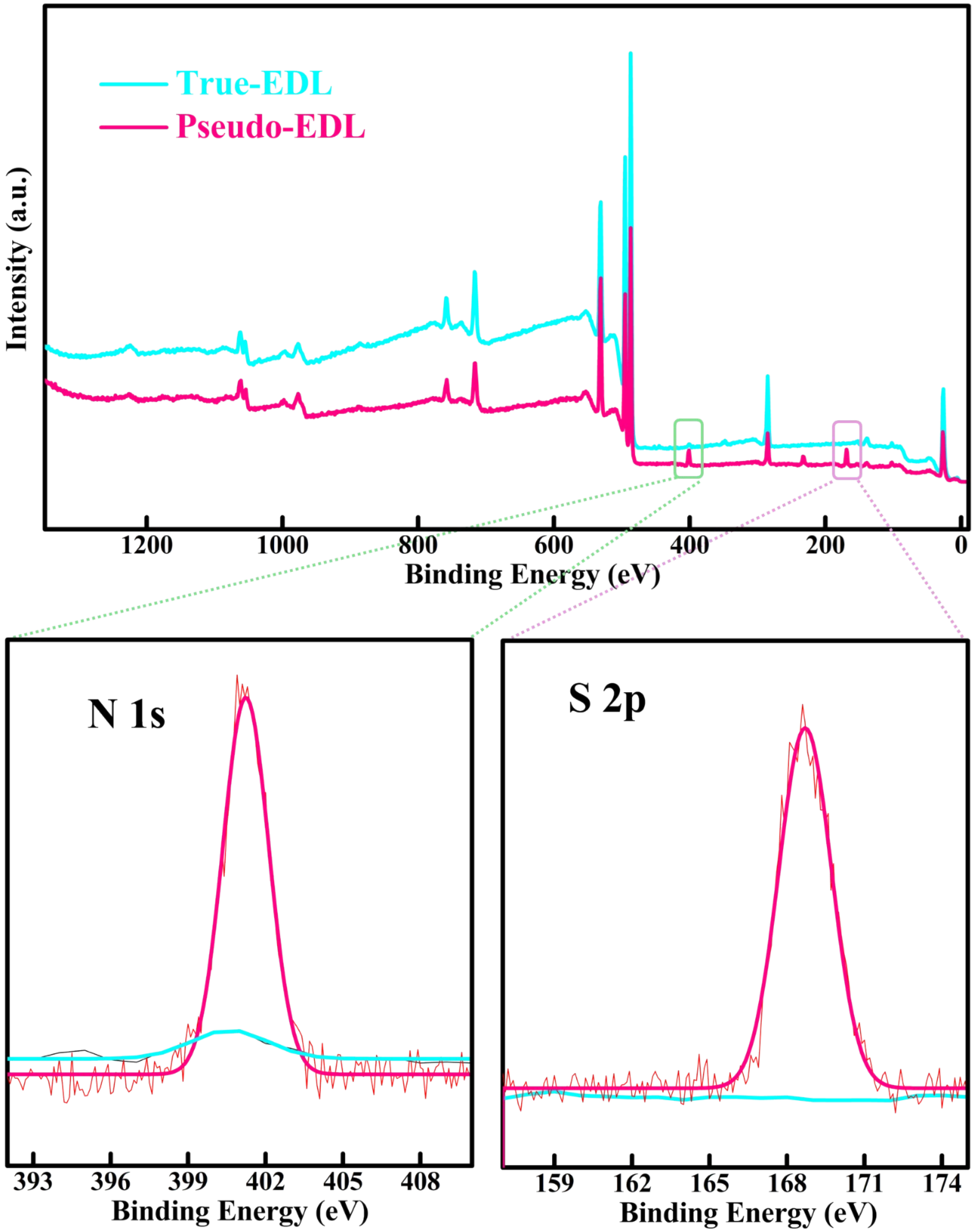

Fig. S8. XPS spectra of true-EDL and pseudo-EDL interfaces show survey scan (top) and high-resolution N 1s and S 2p regions (bottom). Pseudo-EDL exhibits significant peaks at ~400 eV (N 1s) and ~168 eV (S 2p), indicating that aniline oligomers and sulfate species are responsible for electrode degradation.

Supplementary Note 5

Insitu EIS analysis of PVA@Pan

To evaluate the charge transfer mechanism, a PVA@Pan induction layer was sandwiched by two SR layers with edges sealed by uncured fresh SR gel. The air gaps and voids were removed by sucking out air via a micro-diameter needle tip of a hypodermic syringe. A metallic lead is inserted in the induction layer. For evaluation of the dominant mechanism a two-cell EIS setup was used, in which PVA@Pan induction layer was connected to an electrochemical workstation via two platinum wires. Owing to the stratified tissue structure of human skin, keratin, fatty acids, and cholesterol with low water content, were used as the positive electrification and perturbation layer.

The nyquist plot of the imaginary part as a function of the real impedance shows a semicircle impedance pattern for true-EDL which indicates the total contribution from internal resistance with the dominance of PVA@Pan resistance compared to the Pt electrode, as shown in Figure S 9a. The nyquist impedance of pseudo-EDL shows an internal semicircle and diffusion resistance tail along with a low slope line, as shown in the inset of Figure S8a. The low slope demonstrates the dominance of ion diffusion over EDL formation. The absence of equilibrium differential capacitance in both devices indicates the absence of contribution from occluded air or electrification layer impedance. The phase angle profile over a wide range of frequencies manifests the charge transfer pattern in a device, as shown in Figure 3d. In the three regions, 10^{-2}–10^{0} Hz (low-frequency diffusion region), 10^{0}–10^{2} Hz (medium frequency, charge transfer region), and 10^{2}–10^{6} Hz (high frequency, ohmic and inductive region). The activity in the low-frequency region is attributed to equivalent series capacitance and ion diffusion in the matrix. The medium frequency region shows electrostatic displacement of charges or dipole delocalization, which is characteristic of a double layer. The high-frequency region is attributed to ohmic or inductive resistance originating from the internal resistance of the electrode and faradaic charge screening mechanism. While the true-EDL device exhibits faradaic charge transfer, the pseudo-EDL exhibits dominant ion diffusion triggered charge transfer. The same pattern is observed for several devices with induction layers in which the active residual species were, acid, base, salt, multiwalled carbon nanotubes, oxidized metal, and oxidant species, Figure 3c. Further, in a true-EDL device, there are no active residual charges so the modulus resistance, hence capacitance is lesser than the pseudo-EDL device, Figure S 9b-c. The high capacitance in pseudo-EDL is contributed from parasitic capacitive interfaces formed by active residual charges and electrification charges in the induction layer. The results demonstrate that the induction layers with active residual species reduce the density and spread the electrification-induced charges, thereby affecting the electrical output of TEI.

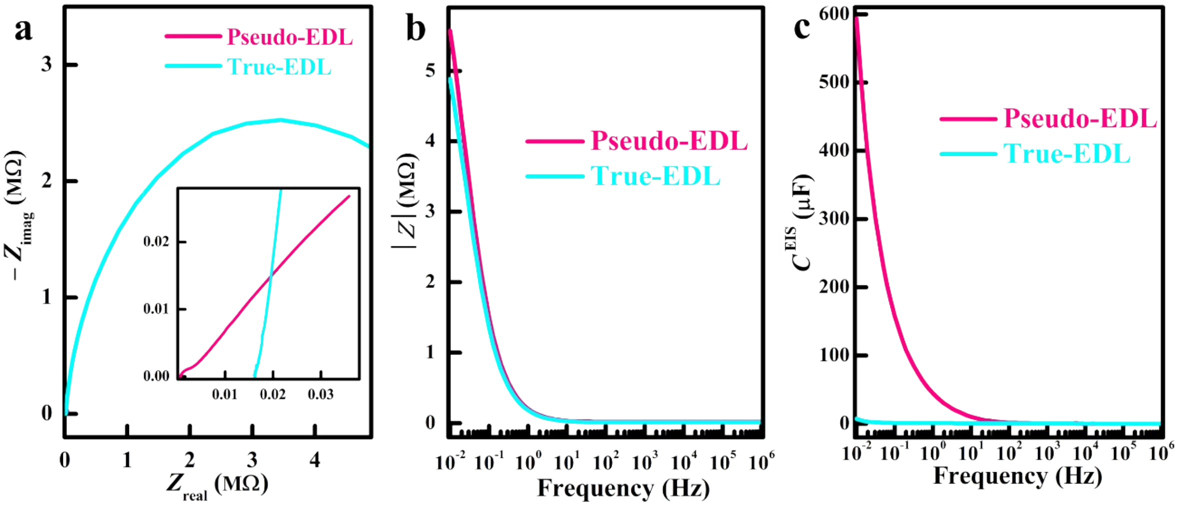

Fig. S9. EIS comparison of ionotronics of various induction layers forming true-EDL and pseudo-EDL interfaces: (a) Nyquist plot, (b) bode modulus, and (c) capacitance (−1/2πfZimag) at frequency range of 10^{-2} –10^{6} Hz.

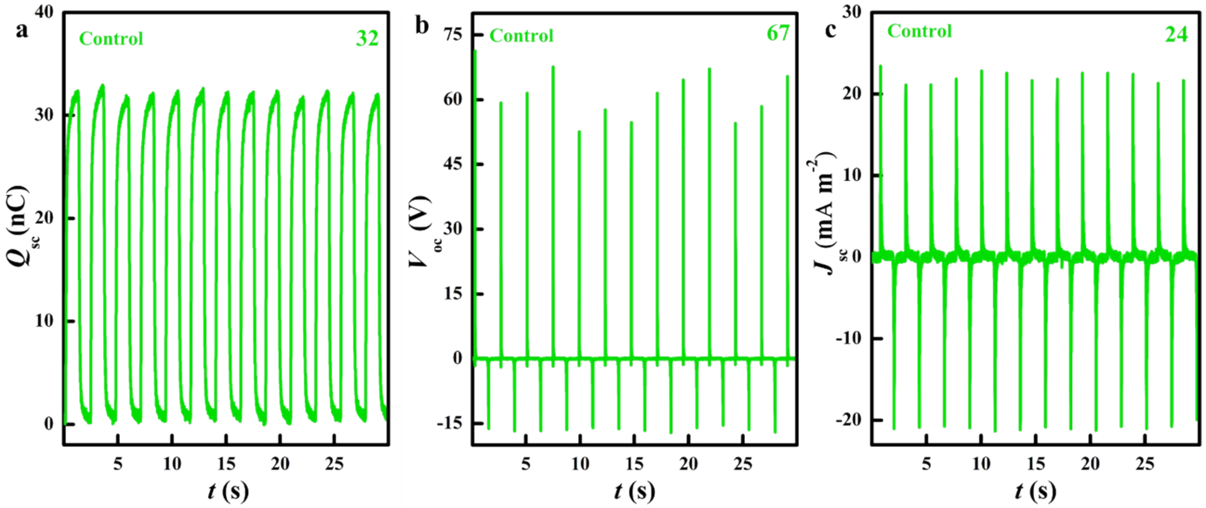

Fig. S10. Electrical output of control TEI with pristine PVA as an induction layer.

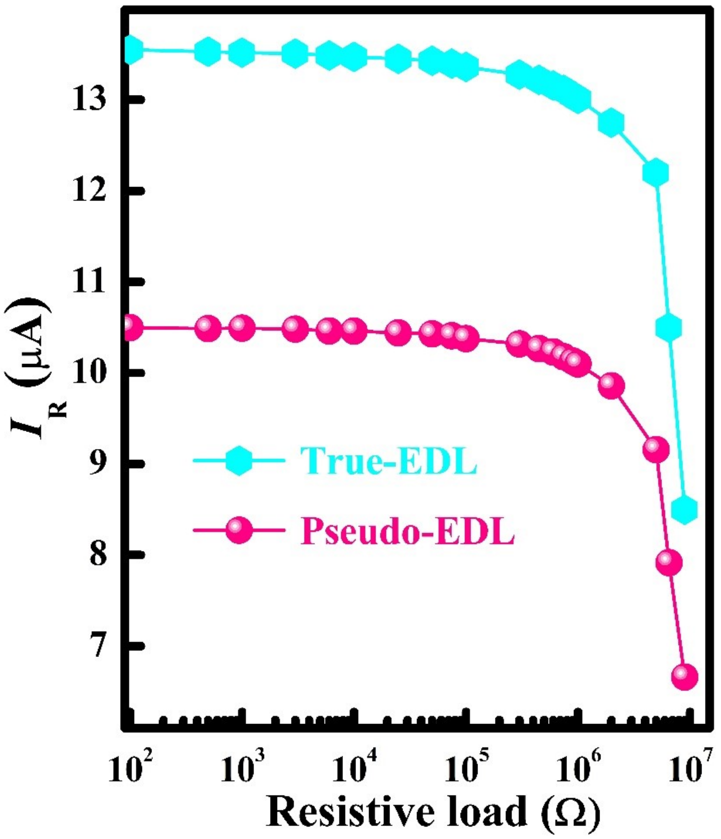

Fig. S11. Current profile of TEI under external resistive load.

Table S2. interfacial charge transfer parameters for true-EDL and pseudo-EDL systems from EIS.

Parameter	true-EDL	pseudo-EDL
Resistance (R)	12000 Ω	47000 Ω
Conductivity (σ)	0.023 S m^{-1}	0.01 S m^{-1}
CPE Exponent (n)	0.95	0.75
CPE Magnitude	0.35 μF	0.08 μF
Phase Angle (θ) at 1 Hz	79 °	43 °
Frequency at Minimum Impedance	1 kHz	100 Hz

Supplementary Note 6

Electrical performance stability and durability

Figure S12 illustrates the long-term electrical and mechanical stability of the PVA@Pan-based triboelectric ionotronic device. The open-circuit voltage (Voc) profiles measured on Day 1, Day 25, and Day 50 consistently exhibit sharp and stable voltage peaks around ~168 V, indicating excellent retention of output performance over extended periods as shown in Figure S12a. The inset photographs demonstrate the robustness of PVA@Pan, which serves as the optimal induction layer material due to its minimal energy losses. Notably, the PVA@Pan solution was stored in a beaker for 8 months, and even after this duration, a sample extracted from the bulk remained soft, flexible, and capable of fully recovering its shape after mechanical deformation, indicating that the crosslinking between PVA and Pan remains intact. The images also show the assembled TEI and its flexible, conductive properties. Furthermore, the device's operational stability during continuous cycling for approximately 1600 seconds (Figure S12b), where Voc output remains steady without notable degradation. These results underscore the long-term stability and mechanical resilience of the PVA@Pan induction layer and TEI, supporting their suitability for energy harvesting and wearable electronics applications.

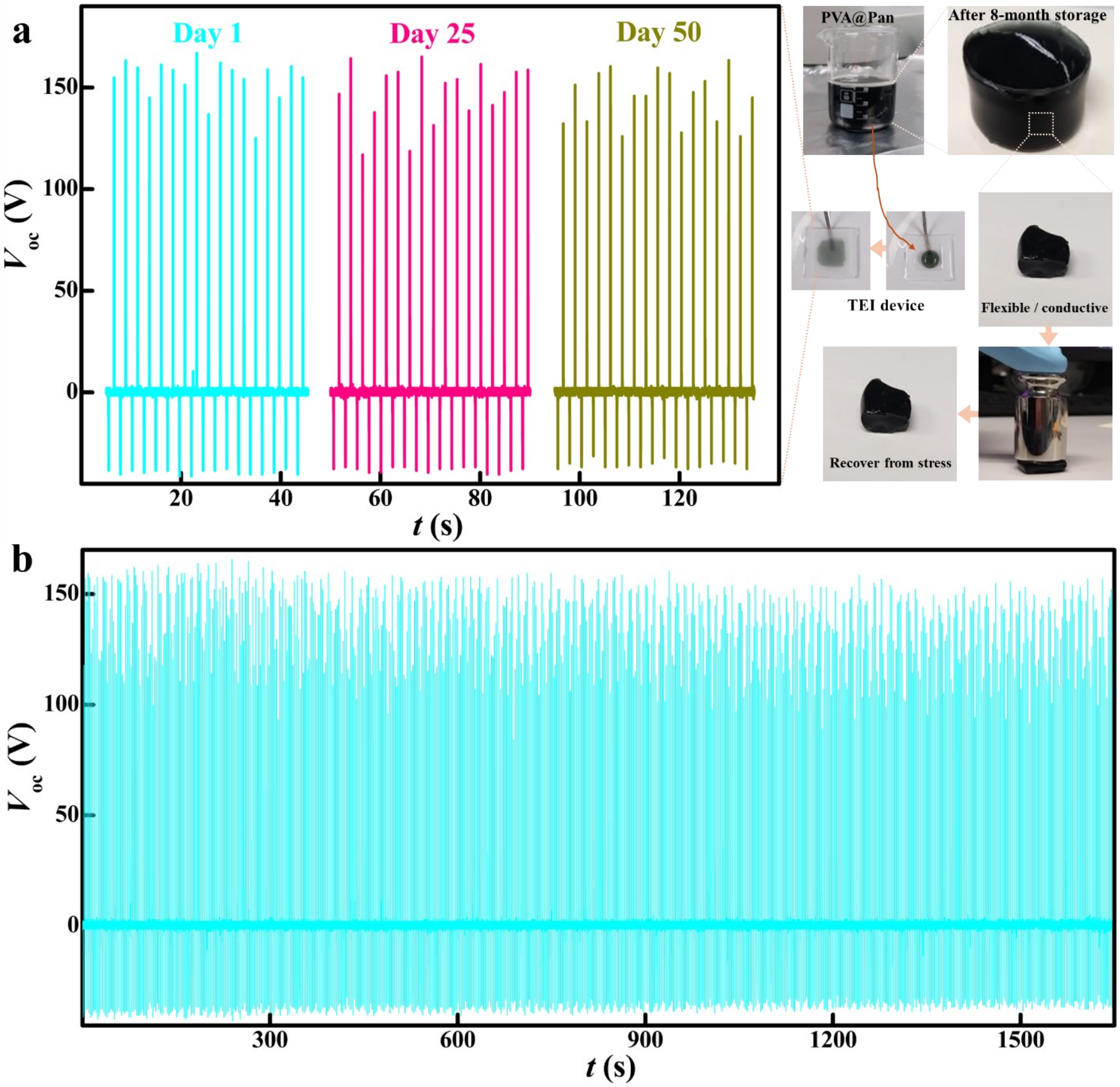

Fig. S12. Long-term stability of TEI. (a) consistent Voc profiles over 50 days with insets demonstrating material durability and (b) stable continuous operation over 1600 seconds.

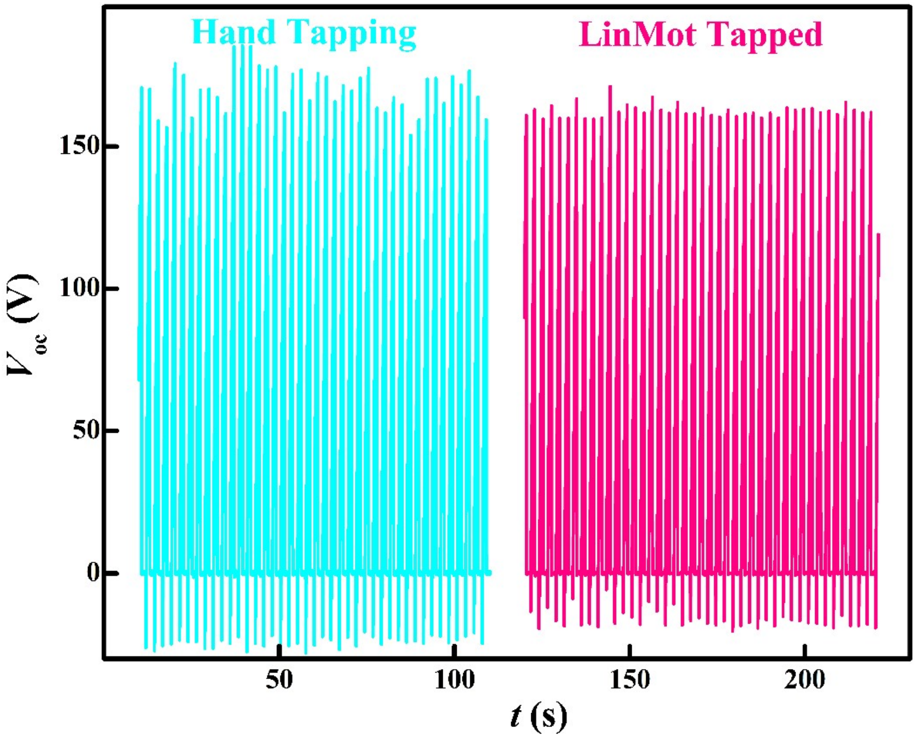

Fig. S13. Comparison of output voltage from hand tapping and linear motor induced contact separation cycles.

Supplementary Note 7

Edge Effects on Voc and Leakage Currents

The observed increase in open-circuit voltage (Voc) with device size stems from reduced edge-induced charge leakage, governed by the inverse relationship between device dimensions and the perimeter-to-area ratio. In smaller devices, air-exposed edges create localized electric field intensification (~3 kV/mm), exceeding the dielectric breakdown threshold of air and triggering corona discharge-a process where ionized air molecules form conductive plasma channels divert triboelectric charges away from the electrode, significantly suppressing Voc. Concurrently, unsealed edges act as pathways for ambient humidity or ionic species (e.g., H^+, Na^+) to penetrate the interface, forming resistive shorts that exacerbate leakage currents, particularly in hydrophilic or hygroscopic systems. In this study, hydrophobic encapsulation (Silicone) was used to suppress fringe field and moisture ingress and thereby modulate the leakage-magnitude. The passivated edges establish a stabilized air layer at the enclosed interface, enabling efficient capacitive energy storage within the induction layer that would otherwise dissipate as parasitic losses. Therefore, as device area increases, the perimeter-to-area ratio decreases exponentially (e.g., ~88% reduction from 1 cm^2 to 12.25 cm^2), minimizing the relative contribution of edge-driven losses with dominant charge transfer mechanism through capacitive storage instead of conventional diffusive leakage. This geometric scaling principle remains consistent across induction layer materials as shown in Figure S14, due to absence of parasitic dissipation through field-driven ionization and ionic shunting.

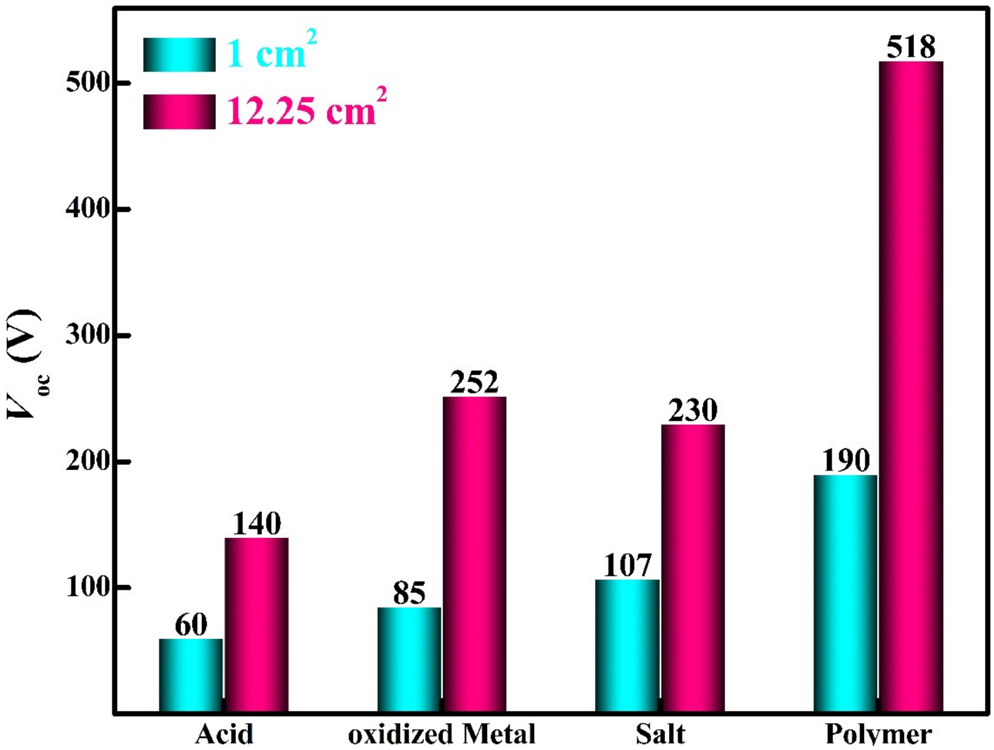

Figure S14. Output voltage enhancement vs. active area scaling with enhanced edge density in various TEI.

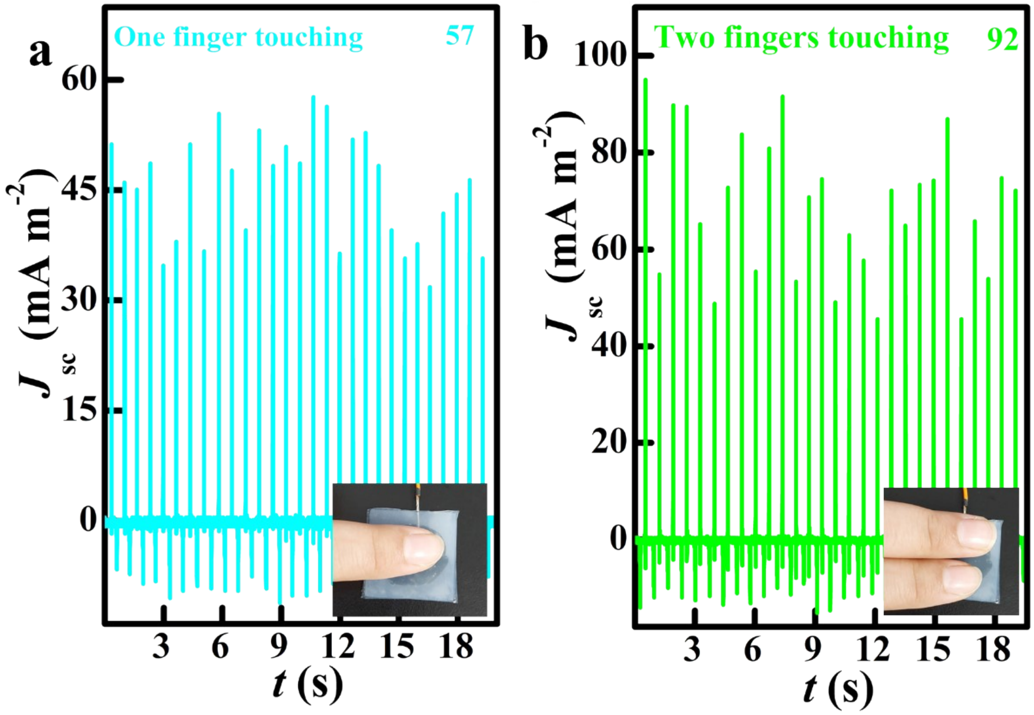

Fig. S15. Demonstration of harvesting biomechanical energy by TEI via slight touching (a) single finger, and (b) two fingers.

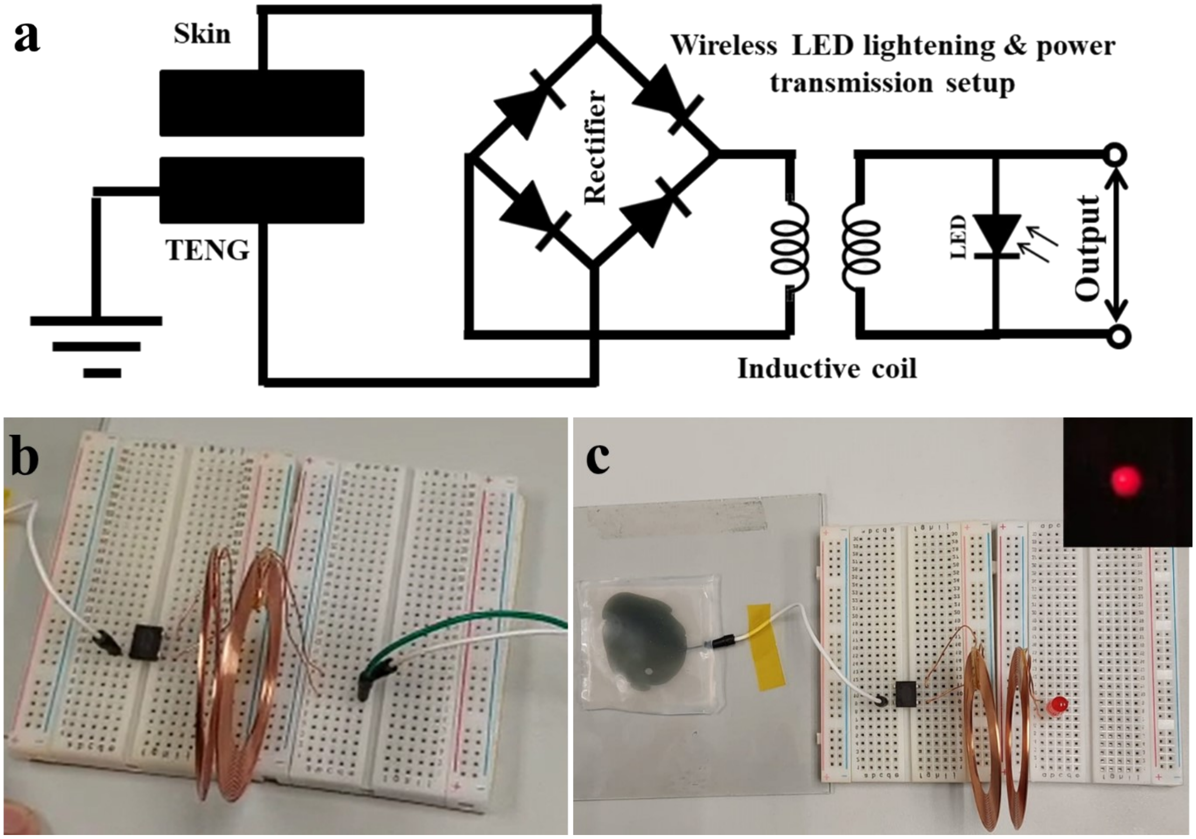

Fig. S16. Demonstration of wireless power transmission to another inductive coil placed at 1 cm distance.

Table S3. Comparison of PVA@Pan based TEI with ionotronics using various types of ionic conductor's *vs* skin counterpart. The cyan highlight indicates that the reported device has lower performance in specific properties compared to devices highlighted in orange.

Induction layer	**State**	**Load (M Ω)**	**Power density (W m^{-2})**	**Input stimuli**	**Ref. #**
ITO	Solid	100	0.500		[1]
Graphene coated Cu	Solid	100	0.0919		[2]
Neoprene/ Silver flakes	Solid	22	0.023	15 N, 1 Hz	[3]
AgNWs	Solid	2	2.66		[4]
MXenes / CNF	Liquid	50	0.5049	2 Hz	[5]
PEDOT: PSS	Liquid	100	0.0021		[6]
Galinstan	Liquid	1000	0.00843		[7]
Saline	Liquid	100	0.0116		[8]
Sulfonated Lignin-Fe^{3+} / PAA	gel	1000	0.053		[9]
Fe^{3+} / Phytic acid / PEDOT: PSS / polylipoic acid	gel	110	0.002		[10]
Borax / PVA	gel	1	0.4		[11]
Borax / PVA	Hydrogel	110	0.005		[12]
Alginate / PAAm	Hydrogel	2400	0.0057		[13]
PAM-hydroxyethyl Cellulose /LiCl	Hydrogel	10	0.626		[14]
Polydopamine /MWCNT /agarose / PVA	Hydrogel	500	0.75		[15]
Poly (Dopamine-Co-acrylamide)	Hydrogel	100	4.3		[16]
Carbon nanotubes / putty	Hydrogel	300	0.41		[17]
Sulfide doped Borax/NaCl /PVA	Hydrogel	100	0.0135		[18]
Ag NWs/PEDOT	Hydrogel	400	0.327		[19]
Gum Arabic/ PAA	Hydrogel	9	11.1	2 N, 1 Hz	[20]
PVA@Pan	Highly viscous gel	5	15.5	1.5 N, 2 Hz	This work

Table S4. Comparison of TEI with prominent PVA-based reported ionotronics. The cyan highlight indicates lower performance in specific properties compared to devices highlighted in orange.

Structure	**Jsc (mA/m^2)**	**Power density (W/m^2)**	**Power density /N (mA/m^{2}N)**	**Matching impedance (MΩ)**	**Input stimuli**	**Ref.#**
PVA-CaCl$_2$ vs PDMS	55	11.3	0.226	30	50 N, 1 Hz	[21]
PVA-Functionalized imidazolium vs. PDMS	61.5	5.2	0.104	40	50 N, 5 Hz	[22]
PVA-CaCl$_2$ vs. PTFE	16.875	1.4	0.357	10	0.4 kgf (3.924 N), 1 Hz	[23]
PVA-PVDF vs. skin	1	0.0461	Na	120	na, 0.75 Hz	[24]
PVA-crystalline silk microparticles vs. Skin	43.25	14.4	2.88	40	5 N, 5Hz	[25]
PVA-PTFE vs. oil-absorbing paper	0.1	0.261	Na	30	2 Hz	[26]
PVA-Mxene nanofiber vs. Silk fibroin nanofibers	18	1.09	0.109	5	10 N, 10 Hz	[27]
PVA-PEI-Au vs. PET	20	17.73	Na	220	na, 1 Hz	[28]
PVA-Cellulose microparticle vs. Kapton	125	84.5	16.9	200	4-5 N, 1Hz	[29]
PVA-LiCl vs PTFE	260	83	1.66	15	50 N, 5 Hz	[30]
PVA-TCNQ vs. PDMS	218	41	8.2	1	5 N, 2 Hz	[31]
PVA-Pan vs. Skin	**303**	**15.5**	**10.33**	**5**	**1.5 N, 2 Hz**	**This work**

Movie S1.
Demonstration of device durability and output stability under mechanical stress.

Movie S2.
A 9 cm^2 PVA@Pan as a power source for lightening ~ 500 LEDs (0.06 W each).

Movie S3.
A 9 cm^2 PVA@Pan as a power source for lightening 104 LEDs (0.5 W each).

Movie S4.
Wireless power transmission via inductive coils placed 1 cm apart.

Movie S5.
Wireless lightening of LED via inductive coils placed 1 cm apart.

References

[1] Y. Yang, H. Zhang, Z.-H. Lin, Y. S. Zhou, Q. Jing, Y. Su, J. Yang, J. Chen, C. Hu, Z. L. Wang, *ACS Nano* **2013**, 7, 9213.

[2] Y. Li, W. Zheng, H. Zhang, H. Wang, H. Cai, Y. Zhang, Z. Yang, *Nano Energy* **2020**, 70, 104540.

[3] S. Hu, S. Chang, G. Xiao, J. Lu, J. Gao, Y. Zhang, Y. Tao, *Advanced Materials Technologies* **2022**, 7, 2100870.

[4] A. Pratap, N. Gogurla, S. Kim, *ACS Applied Electronic Materials* **2022**, 4, 1124.

[5] W.-T. Cao, H. Ouyang, W. Xin, S. Chao, C. Ma, Z. Li, F. Chen, M.-G. Ma, *Advanced Functional Materials* **2020**, 30, 2004181.

[6] J. Shi, X. Chen, G. Li, N. Sun, H. Jiang, D. Bao, L. Xie, M. Peng, Y. Liu, Z. Wen, X. Sun, *Nanoscale* **2019**, 11, 7513.

[7] Y. Yang, N. Sun, Z. Wen, P. Cheng, H. Zheng, H. Shao, Y. Xia, C. Chen, H. Lan, X. Xie, C. Zhou, J. Zhong, X. Sun, S.-T. Lee, *ACS Nano* **2018**, 12, 2027.

[8] X. Wang, Y. Yin, F. Yi, K. Dai, S. Niu, Y. Han, Y. Zhang, Z. You, *Nano Energy* **2017**, 39, 429.

[9] Y. Feng, J. Yu, D. Sun, C. Dang, W. Ren, C. Shao, R. Sun, *Nano Energy* **2022**, 98, 107284.

[10] A. Khan, S. Ginnaram, C.-H. Wu, H.-W. Lu, Y.-F. Pu, J. I. Wu, D. Gupta, Y.-C. Lai, H.-C. Lin, *Nano Energy* **2021**, 90, 106525.

[11] K. Parida, V. Kumar, W. Jiangxin, V. Bhavanasi, R. Bendi, P. S. Lee, *Advanced Materials* **2017**, 29, 1702181.

[12] Y. C. Lai, H. M. Wu, H. C. Lin, C. L. Chang, H. H. Chou, Y. C. Hsiao, Y. C. Wu, *Advanced Functional Materials* **2019**, 29, 1904626.

[13] B. Ying, R. Zuo, Y. Wan, X. Liu, *ACS Applied Electronic Materials* **2022**, 4, 1930.

[14] D. Bao, Z. Wen, J. Shi, L. Xie, H. Jiang, J. Jiang, Y. Yang, W. Liao, X. Sun, *Journal of Materials Chemistry A* **2020**, 8, 13787.

[15] Q. Guan, G. Lin, Y. Gong, J. Wang, W. Tan, D. Bao, Y. Liu, Z. You, X. Sun, Z. Wen, *Journal of Materials Chemistry A* **2019**, 7, 13948.

[16] Y. Long, Y. Chen, Y. Liu, G. Chen, W. Guo, X. Kang, X. Pu, W. Hu, Z. L. Wang, *Nanoscale* **2020**, 12, 12753.

[17] Y. Chen, X. Pu, M. Liu, S. Kuang, P. Zhang, Q. Hua, Z. Cong, W. Guo, W. Hu, Z. L. Wang, *ACS nano* **2019**, 13, 8936.

[18] W. Xu, M.-C. Wong, Q. Guo, T. Jia, J. Hao, *Journal of Materials Chemistry A* **2019**, 7, 16267.

[19] J. Sun, X. Pu, M. Liu, A. Yu, C. Du, J. Zhai, W. Hu, Z. L. Wang, *ACS nano* **2018**, 12, 6147.

[20] I. Firdous, M. Fahim, F. Mushtaq, W. A. Daoud, *Nano Energy* **2023**, 108817.

[21] J. Y. Cheong, J. S. C. Koay, R. Chen, K. C. Aw, T. S. Velayutham, B. Chen, J. Li, C. Y. Foo, W. C. Gan, *Nano Energy* **2021**, 90, 106616.

[22] P. C. Uzabakiriho, Z. Haider, K. Emmanuel, R. u. S. Ahmad, A. Haleem, U. Farooq, J. D. D. Uwisengeyimana, M. K. Mbogba, A. Fareed, K. Memon, I. Khan, P. Hu, G. Zhao, *Advanced Materials Technologies* **2020**, 5, 2000303.

[23] H. Ryu, J.-H. Lee, T.-Y. Kim, U. Khan, J. H. Lee, S. S. Kwak, H.-J. Yoon, S.-W. Kim, *Advanced Energy Materials* **2017**, 7, 1700289.

[24] W. Du, J. Nie, Z. Ren, T. Jiang, L. Xu, S. Dong, L. Zheng, X. Chen, H. Li, *Nano Energy* **2018**, 51, 260.

[25] B. Dudem, S. A. Graham, R. D. I. G. Dharmasena, S. R. P. Silva, J. S. Yu, *Nano Energy* **2021**, 83, 105819.

[26] J.-P. Wu, W. Liang, W.-Z. Song, L.-N. Zhou, X.-X. Wang, S. Ramakrishna, Y.-Z. Long, *Nanoscale* **2020**, 12, 23225.

[27] C. Jiang, C. Wu, X. Li, Y. Yao, L. Lan, F. Zhao, Z. Ye, Y. Ying, J. Ping, *Nano Energy* **2019**, 59, 268.

[28] L. Wang, X. Yang, W. A. Daoud, *Nano Energy* **2019**, 55, 433.

[29] S. A. Graham, B. Dudem, A. R. Mule, H. Patnam, J. S. Yu, *Nano Energy* **2019**, 61, 505.

[30] L. Shi, S. Dong, H. Xu, S. Huang, Q. Ye, S. Liu, T. Wu, J. Chen, S. Zhang, S. Li, X. Wang, H. Jin, J. M. Kim, J. Luo, *Nano Energy* **2019**, 64, 103960.

[31] L. Wang, Y. Wang, X. Bo, H. Wang, S. Yang, X. Tao, Y. Zi, W. W. Yu, W. J. Li, W. A. Daoud, *Advanced Functional Materials* **2022**, 32, 2204304.